Materials Futures

PAPER • **OPEN ACCESS**

Improving cycling performance of the $NaNiO_2$ cathode in sodium-ion batteries by titanium substitution

To cite this article: Siyu An *et al* 2024 *Mater. Futures* **3** 035103

OPEN ACCESS
IOP Publishing | Songshan Lake Materials Laboratory
Materials Futures
Mater. Futures 3 (2024) 035103 (16pp)
https://doi.org/10.1088/2752-5724/ad5faa

Improving cycling performance of the $NaNiO_2$ cathode in sodium-ion batteries by titanium substitution

Siyu An[1], Leonhard Karger[1], Sören L Dreyer[1], Yang Hu[2], Eduardo Barbosa[1], Ruizhuo Zhang[1], Jing Lin[1], Maximilian Fichtner[2], Aleksandr Kondrakov[1,3], Jürgen Janek[1,4,*] and Torsten Brezesinski[1,*]

[1] Battery and Electrochemistry Laboratory (BELLA), Institute of Nanotechnology, Karlsruhe Institute of Technology (KIT), Kaiserstr. 12, 76131 Karlsruhe, Germany
[2] Helmholtz Institute Ulm (HIU) Electrochemical Energy Storage, Helmholtzstr. 11, 89081 Ulm, Germany
[3] BASF SE, Carl-Bosch-Str. 38, 67056 Ludwigshafen, Germany
[4] Institute of Physical Chemistry & Center for Materials Research (ZfM/LaMa), Justus-Liebig-University Giessen, Heinrich-Buff-Ring 17, 35392 Giessen, Germany

E-mail: juergen.janek@kit.edu and torsten.brezesinski@kit.edu

Received 12 April 2024, revised 18 June 2024
Accepted for publication 26 June 2024
Published 25 July 2024

Abstract

O3-type layered oxide cathodes, such as $NaNi_{0.5}Mn_{0.5}O_2$, have garnered significant attention due to their high theoretical specific capacity while using abundant and low-cost sodium as intercalation species. Unlike the lithium analog ($LiNiO_2$), $NaNiO_2$ (NNO) exhibits poor electrochemical performance resulting from structural instability and inferior Coulomb efficiency. To enhance its cyclability for practical application, NNO was modified by titanium substitution to yield the O3-type $NaNi_{0.9}Ti_{0.1}O_2$ (NNTO), which was successfully synthesized for the first time via a solid-state reaction. The mechanism behind its superior performance in comparison to that of similar materials is examined in detail using a variety of characterization techniques. NNTO delivers a specific discharge capacity of ~190 mAh g^{-1} and exhibits good reversibility, even in the presence of multiple phase transitions during cycling in a potential window of 2.0−4.2 V vs. Na^+/Na. This behavior can be attributed to the substituent, which helps maintain a larger interslab distance in the Na-deficient phases and to mitigate Jahn–Teller activity by reducing the average oxidation state of nickel. However, volume collapse at high potentials and irreversible lattice oxygen loss are still detrimental to the NNTO. Nevertheless, the performance can be further enhanced through coating and doping strategies. This not only positions NNTO as a promising next-generation cathode material, but also serves as inspiration for future research directions in the field of high-energy-density Na-ion batteries.

* Authors to whom any correspondence should be addressed.

Supplementary material for this article is available online

Keywords: Ni-rich layered oxide, cathode material, substitution, doping, electro-chemo-mechanical degradation, Na-ion battery

1. Introduction

With the rapid development of lithium-ion batteries (LIBs), both electric vehicles and large-scale energy storage systems have experienced significant advancements [1–3]. However, due to the uneven distribution of lithium resources and cost considerations, there is an urgent need for novel, more sustainable solutions to meet future demands. Because of similarities in the storage mechanisms between sodium-ion batteries (SIBs or NIBs) and LIBs and the higher abundance and widespread distribution of sodium in the Earth's crust, as well as in the seawater, SIBs have the potential to become a next-generation (low-cost) technology in the field of electrochemical energy storage [4–6]. Among numerous SIB cathode materials, layered transition metal oxides, Na_xTMO_2 (TM = Ni, Co, Mn, Fe, Cr, etc), stand out as the most promising candidates due to their high theoretical specific capacities and high operation potentials, similar to the successfully utilized $LiTMO_2$ (e.g. $LiNi_xCo_yMn_zO_2$, referred to as NCMs or NMCs) in LIBs [6–10].

Transition metal oxide cathode materials in SIBs exist mostly in two thermodynamically stable structures, known as O3 (Na^+ on octahedral sites coordinated by oxygen) and P2 (Na^+ on prismatic sites) [3, 11–13]. In the O3-type structure, Na^+ diffuses between adjacent NaO_6 octahedra through interstitial tetrahedral sites, leading to a relatively higher energy barrier compared to P2-type structures, and therefore to inferior rate capability. In the P2-type structure, sodium transport occurs via face-shared trigonal prismatic sites, resulting in better diffusivity. Nevertheless, the higher sodium content of O3-type compounds and the resulting higher storage capacity make them more attractive for practical (full cell) applications [6, 7, 13, 14].

In LIBs, to achieve high specific capacities ($q_{ch/dis} \geqslant 200$ mAh g^{-1}) in a reasonable potential range, the focus is strongly placed on layered Ni-rich oxides (>80% Ni fraction), such as $LiNiO_2$ (LNO) [15–19]. However, due to the relatively close ionic radii of Li^+ ($r = 0.76$ Å) and Ni^{2+} ($r = 0.69$ Å), Ni_{Li} point defects (Ni^{2+} occupying crystallographic Li sites) form during calcination, which is generally believed to be detrimental to the electrochemical behavior [20–23]. Inspired by the high capacity achievable with LNO, O'3-type $NaNiO_2$ (NNO) in SIBs is also widely investigated (owing to both its high operating potential and high theoretical specific capacity of 235 mAh g^{-1}) [24–26]. Na^+ ($r = 1.02$ Å) has a significantly different ionic radius compared to Ni^{2+} and Ni^{3+} ($r = 0.56$ Å), which prevents the formation of substitutional (interlayer) defects, but causes larger volume variations during cycling [22, 27–29].

Due to the larger ionic radius of Na^+, NNO experiences in-plane TMO_2 slab gliding during the intercalation and extraction of sodium ions, which in turn can lead to multiple, poorly reversible phase transitions (O'3 → P'3 → P"3 → O"3 → O"'3). Aside from that, low-spin Ni^{3+} ($t_{2g}{}^6e_g{}^1$) induces strong Jahn–Teller distortion, leading to strain and ultimately resulting in capacity fading [7, 13, 14, 24, 25]. In 2013, Vassilaras *et al* reported on the extraction of 0.85 Na^+ (equivalent to $q_{ch} \approx 199$ mAh g^{-1}) and re-insertion of 0.62 Na^+ (equivalent to $q_{dis} \approx 147$ mAh g^{-1}) in NNO during the initial cycle in a potential window of 2.0−4.5 V vs. Na^+/Na [24]. However, the low Coulomb efficiency indicates that further research is required to address the challenges associated with the potential use of NNO. Komaba *et al* conducted a comprehensive study on $NaNi_{0.5}Mn_{0.5}O_2$, where divalent Ni^{2+} is oxidized to tetravalent Ni^{4+} during charging, and the electrochemically inactive Mn^{4+} contributes to structural stability [30]. Inspired by this work, Yu *et al* proposed that Ti^{4+} could play a similar role to Mn^{4+} and successfully incorporated Ti^{4+} into the crystallographic Ni position, resulting in the formation of rhombohedral (α-$NaFeO_2$-type) $NaNi_{0.5}Ti_{0.5}O_2$. Electrochemical testing revealed a reversible specific capacity of 121 mAh g^{-1} at a rate of 0.2C [31]. Maletti *et al* further probed $NaNi_{0.5}Ti_{0.5}O_2$ using *operando* synchrotron x-ray diffraction measurements, demonstrating that titanium remains tetravalent throughout cycling and the gliding of TMO_2 slabs is strongly suppressed. This led to a reversible transition between the O3 and P3 phases (1.5−4.2 V vs. Na^+/Na), exhibiting a much smoother voltage profile than that of NNO [32]. Even though $NaNi_{0.5}Ti_{0.5}O_2$ shows superior cycling stability over NNO, the low reversible capacity leaves room for improvements.

In addition to doping/substitution, the synthesis conditions for layered oxides, particularly the calcination temperature, play a significant role in the material's performance. In the case of LIBs, it has been found that the calcination temperature has a critical influence on the electrochemical performance of $Li_{1.2}Mn_{0.56}Ni_{0.16}Co_{0.08}O_2$ [33]. Similarly, for SIBs, the choice of synthesis temperature can lead to the formation of either α-$NaMnO_2$ at a lower temperature or β-$NaMnO_2$ at a higher temperature [34, 35]. Moreover, the Na/TM ratio also has a notable effect on the material's performance. Some studies have proposed using excess sodium to compensate for losses during calcination, thereby achieving the desired stoichiometry [36, 37]. However, Zhou *et al* discovered that a slight sodium deficiency can have beneficial effects on the initial capacity and capacity retention [38]. Furthermore, layered oxides are sensitive to the cooling rate (as part of the synthesis). In LIBs, Liu *et al* explored the

correlation between cooling rate, calcination conditions, and the generation of Ni/Mn disorder and oxygen vacancies in the spinel $LiNi_{0.5}Mn_{1.5}O_4$ [39]. Their research demonstrated that a slow cooling rate, combined with annealing steps, effectively mitigates the formation of oxygen vacancies and impurity phases. However, the findings indicate that a certain fraction of oxygen vacancies is required for achieving high performance. Similarly, in SIBs, the cooling rate plays a pivotal role. Liu *et al* enhanced the capacity by quenching the Mn-based material $Na_{2/3}M_xMn_{1-x}O_2$ (M = dopant) in liquid nitrogen to achieve a vacancy-free structure [40]. Xu *et al* also proposed the significance of native lattice stress induced by quenching on the fading behavior [41]. In general, variations of parameters during the calcination process appear to have a significant impact on both the material's structure and performance, yet quantitative knowledge is lacking.

In the present work, we consider $NaNi_{0.9}Ti_{0.1}O_2$ (NNTO) as a potentially new cathode material for application in SIBs. We have investigated different synthesis conditions in a systematic manner and analyzed the resulting structures, particle morphologies, and electrochemical properties of the obtained samples. Through optimization of the preparation conditions, NNTO of high purity (>98%) was produced, which delivered higher specific capacity (∼190 mAh g^{-1} at C/30 rate in the potential window of 2.0−4.2 V vs. Na^+/Na) and showed better cycling stability than NNO and titanium-rich $NaNi_{0.5}Ti_{0.5}O_2$ [25, 26, 31, 32, 37]. However, NNTO still suffers from degradation upon battery operation. By combining physical and electrochemical characterization techniques, we gain insight into the potential reasons behind the capacity fading, which provides new avenues for tailoring this promising cathode material.

2. Experimental section

2.1. Synthesis

$NaNi_{0.9}Ti_{0.1}O_2$ was prepared by a two-step solid-state reaction from $Ni(OH)_2$ ($d_{50} \approx 4$ μm, BASF SE), nanoscale TiO_2, and reagent-grade NaOH powder (97%; Sigma-Aldrich). For the initial pre-calcination, the reactants were homogenized under Ar atmosphere for 10 min with different molar equivalents of NaOH, namely 1.0, 1.025, and 1.05, i.e. n(TM)/n(Na) = 1:1, 1:1.025, and 1:1.05, respectively, using a laboratory blender (Kinematica). The precursor mixture was then heated in an alumina crucible under O_2 flow (1.4 l h^{-1}) in a tube furnace (Nabertherm P330) at 300 °C for 10 h with 3 K min^{-1} heating and cooling rates. After cooling to room temperature, the intermediate product was homogenized again for 10 min, followed by transfer to an alumina crucible for the main calcination under different O_2 flow rates of 1.4 and 7 l h^{-1} at temperatures ranging from 600 °C to 900 °C for 12 h with 3 K min^{-1} heating rate and different cooling rates of 2 K min^{-1}, 0.5 K min^{-1}, and quenching. For quenching, the quartz tube containing the sample was directly removed from the furnace and rapidly cooled to room temperature.

For the study of different molar Ni/Ti ratios (95:5, 90:10, 85:15, and 80:20), the molar TM/Na ratio was set to 1:1. Powder mixtures were prepared by blending and pre-calcination, as described above. The homogenized mixtures were calcined under O_2 flow (7 l h^{-1}) at 800 °C for 12 h with 3 K min^{-1} heating rate and 2 K min^{-1} cooling rate.

$NaNiO_2$ was also prepared by solid-state reaction from $Ni(OH)_2$ and NaOH (10 mol.% excess) at 700 °C for 12 h using the above-mentioned conditions.

2.2. Surface coating

An oven-dried Schlenk flask with a magnetic stirring bar was transferred into the glovebox, and 7 ml of dry toluene (Sigma-Aldrich) was added to the flask. Subsequently, 2 M trimethylaluminum (TMA) in toluene (Sigma-Aldrich) was added dropwise (given in equivalents of a base amount of 100 μmol TMA per 1 g of cathode material), and the solution was stirred for 1 h before adding 1 g of cathode material. After 2 h, the flask was transferred to a Schlenk line equipped with a cold trap between the line and flask to remove the solvent under vacuum. Once no liquid phase was visible anymore, the flask was directly connected to the Schlenk line, and the cathode material was dried at room temperature and 1×10^{-3} mbar overnight. Lastly, the product was heated at 300 °C for 1 h under oxygen flow in a tube furnace (Nabertherm P330). The heating and cooling rates were set to 3 K min^{-1}.

2.3. Electrochemical testing

Electrodes were prepared by casting an N-methyl-pyrrolidone (NMP) slurry with 94 wt.% cathode material, 3 wt.% Super C65 carbon, and 3 wt.% polyvinylidene difluoride (Solef 5130; Solvay) binder onto 0.03 mm Al foil as the current collector. The slurry was prepared by combining all components with 20 wt.% additional NMP in a planetary centrifuge mixer (Thinky ARE-250), applying a two-step program with 3 min at 2000 rpm and 3 min at 400 rpm. The slurry was spread onto the current collector using a film applicator (Coatmaster 510; Erichsen) at a rate of 5 mm s^{-1}. The as-made tapes were dried overnight in a vacuum at 120 °C and then calendared at 14 N mm^{-1} (Sumet Messtechnik). Electrodes of 13 mm diameter and 9−12 mg cm^{-2} areal loading were punched out. 95 μl of a 1 M solution of $NaClO_4$ in ethylene carbonate (EC), dimethyl carbonate (DMC), and propylene carbonate (PC), 1:1:1 by vol., containing 5 vol.% fluoroethylene carbonate (FEC) as additive was used as the electrolyte. In a variation, the electrolyte contained no FEC. Subsequently, the prepared electrodes, GF/D glass fiber separator, Na metal, and electrolyte were assembled into 2032-type coin half-cells in an Ar glovebox. Electrochemical testing was done in a potential window of 2.0−4.2 V vs. Na^+/Na at various C-rates (1C = 200 mA g^{-1}).

2.4. X-ray diffraction

XRD data were collected in Debye–Scherrer geometry using a STOE STADI-P diffractometer equipped with a DECTRIS MYTHEN 1K strip detector and a Mo anode ($\lambda = 0.70926$ Å,

50 kV, 40 mA). The instrumental contribution to peak broadening was determined by measuring a NIST 660c LaB_6 standard as a line broadening reference. The samples for XRD were flame-sealed in borosilicate capillaries of 0.5 mm inner diameter and 0.01 mm wall thickness (Hilgenberg).

2.5. Operando XRD

The positive and negative caps and the spacers of the coin-cell casings were subject to modification by electro-erosion machining for *operando* XRD measurements, resulting in a 5 mm diameter hole in the center. The outer holes were sealed with Kapton windows of 6 mm diameter. The cells were cycled at a rate of C/20 utilizing a Gamry Interface 1000 potentiostat. XRD patterns were collected within an angular range of $5° < 2\theta < 37°$ with an acquisition time of about 10 min utilizing the aforementioned STOE Stadi-P diffractometer. The patterns were analyzed according to the Rietveld method using the GSAS-II software [42].

2.6. In situ *XRD*

XRD using a customized diffractometer was used to study the main calcination process; the setup is reported elsewhere [43]. For sample preparation, the pre-calcination mixture for $NaNi_{0.9}Ti_{0.1}O_2$ with 1:1 TM/Na ratio was employed. The mixture was heated at a rate of 1 K min^{-1} under an O_2 atmosphere, with each pattern being the accumulated signal over 5 min. Temperature calibration was performed by comparison with the cell volume of Al_2O_3, which was measured in a separate experiment.

2.7. Scanning electron microscopy

SEM analysis was performed at an accelerating voltage of 10 kV using a LEO-1530 microscope (Carl Zeiss AG) with a field emission source. For cross-sectional imaging, an IB-19510CP polisher (JEOL Ltd) with an Ar-gas source was employed.

2.8. Transmission electron microscopy

Samples for low-magnification TEM imaging and energy-dispersive x-ray spectroscopy (EDS) analysis were embedded in resin in an Ar glovebox to prevent sample degradation. The material was then cut by ultramicrotomy under dry conditions and directly investigated. During preparation, the samples were exposed to air for about 10 min. Samples for atomic resolution analysis were prepared by Ga-focused ion beam (FIB) milling using a Helios 5 CX DualBeam (Thermo Fisher Scientific) and directly transferred to the microscope to minimize exposure to air. The samples were examined using a probe-corrected Themis Z (3.1; Thermo Fisher Scientific) in high-angle annular dark-field (HAADF) scanning transmission electron microscopy (STEM) mode at 300 kV. The chemical composition was examined with the integrated SuperX G2 EDS detector. The data were analyzed using the Velox 3.10 software.

2.9. Inductively coupled plasma-optical emission spectroscopy

The elemental composition was studied by ICP-OES using a Thermo Fisher Scientific ICAP 7600 DUO instrument. Powder samples were dissolved in an acid digester within a graphite furnace. Mass fractions were derived from three independent measurements for each sample of which about 10 mg were dissolved in a mixture of 6 ml hydrochloric acid and 2 ml nitric acid at 353 K for 4 h. The digested samples were diluted for analysis utilizing four different calibration solutions and an internal standard (Sc). The oxygen content was determined by carrier gas hot extraction with a commercial oxygen/nitrogen analyzer TC600 (LECO Corp.). Certified standard KED-1025 was employed for calibration.

2.10. X-ray absorption spectroscopy

XAS at the Ni K-edge was performed in transmission mode using a laboratory Rowland-circle based instrument (easyXAFS300+; easyXAFS, LLC). The Ag x-ray tube was operated at 35 kV, and a Si(444) crystal analyzer was employed [44]. Pristine powder samples were diluted with cellulose and pelletized by a hydraulic press in an Ar glovebox. The prepared pellets were sealed with Kapton tape and then taken out for XAS measurements under ambient atmosphere. Reference NiO and $Ni(OH)_2$ were prepared in a similar fashion. Cycled electrodes (two cycles at C/30 and 8 cycles at C/10) were measured by pre-sealing them in the glovebox using Kapton tape. Energy grids of 2 eV, 0.25 eV, and 0.05 $Å^{-1}$ were used for the pre-edge, near-edge, and post-edge regions, respectively. Multiple scans were collected for the reference Ni foil (Goodfellow or Exafs Materials) and each sample. The absorption spectra were obtained using a Python-based software with integrated dead-time correction (easyXAFS, LLC), according to the relation $\mu(E) \approx \ln(I_0/I_t)$. Energy calibration was based on the first peak in the first derivative of $\mu(E)$ of the Ni reference foil. XAS data were further analyzed using the Demeter package. The normalization energy range was set up to 8800 eV, employing the normalization order 2 within $k = 0$–12 $Å^{-1}$.

2.11. Acoustic emission

AE signals were acquired using a differential wideband sensor (125−1000 kHz; MISTRAS Group) mounted to the bottom of coin cells using vacuum grease to improve contact. The experimental setup also incorporated an in-line pre-amplifier and a data acquisition system (USB AE Node; MISTRAS Group). The pre-amplifier gain, analog filter, and sampling rate were set to 40 dB, 20–1000 kHz, and 5 MSPS, respectively. Sensor coupling was verified by the pencil-lead break test [45, 46]. A minimum of two samples was tested to ensure reproducibility. Initially, the recorded data underwent pre-processing via the AEwin software (MISTRAS Group), involving removal of background noise by excluding all hits with less than two counts, peak frequencies below 100 kHz, and/or amplitudes of less than 27 dB. Subsequently, the data were analyzed in

conjunction with the corresponding electrochemical measurements (one cycle at C/30 and four cycles at C/10).

2.12. Differential electrochemical mass spectrometry

Customized DEMS cells using a 30 mm diameter cathode (with 10 mg cm^{-2} areal loading) were cycled at a rate of C/10. A 4 mm diameter hole in the center of the cathode allowed for gas flow. GF/D, Na metal, and 700 μl of 1.0 M $NaClO_4$ in EC:DMC:PC with FEC were used as the separator, anode, and electrolyte, respectively. During cycling, a constant stream of He carrier gas (purity 6.0, 2.5 ml min^{-1}) was passed through the cells. The extracted gas mixture was probed using a mass spectrometer (OmniStar GSD 320, Pfeiffer Vacuum GmbH). More details can be found in the literature [47, 48].

3. Results and discussion

Since the calcination temperature is crucial for the synthesis of layered oxides, a systematic study of its influence was first carried out. Prior to the main calcination step, a well-blended mixture of 4 μm $Ni(OH)_2$ particles (figure S1(a)), NaOH, and nano-sized TiO_2 was heated at 300 °C under O_2 atmosphere for 10 h (see Experimental section for more details) to facilitate dehydration and ensure good contact between the reactants. The resultant sample was probed using XRD (figure S1(b)). The main reflections matched the rocksalt-type NiO phase. The remaining weaker reflections did neither match the pattern of NaOH nor that of TiO_2. Instead, they can be attributed to a layered structure of $Na_{4x}Ti_{1-x}O_2$ (referred to as $Na_xTi_yO_z$ in the following) formed by solid-state reaction between NaOH and TiO_2 [49]. Notably, the latter side phase was largely amorphous, due to the relatively low pre-calcination temperature.

To determine the optimal temperature range for the main calcination step, an *in situ* XRD measurement was conducted on the pre-heated precursor mixture. The setup used is illustrated in figure S2(a) [43]. During the continuous heating process, *C*2/*m*, *R*−3*m*, and *Fm*−3*m* phases were identified. Figure 1 shows that NiO (*Fm*−3*m*) remains the dominant phase up to 630 °C. However, alongside NiO, the above-mentioned $Na_xTi_yO_z$ was observed, with its structure exhibiting temperature-dependent variations. From 630 °C on, the formation of the layered structure of NNTO with the space group *R*−3*m* is apparent, which persists until 870 °C. As shown in figures 1 and S2(b), with further temperature increase, the reflections of both NNO (*C*2/*m*), such as (20−2), (111), (021), and (221), and NiO become dominant. Additionally, the intensity of the (104) reflection of NNTO decreases. This indicates that NNTO undergoes decomposition into NNO and NiO at higher temperatures. As a result, we determined that the desired *R*−3*m* phase (NNTO) can be achieved in the temperature range of about 630 °C−870 °C.

For verification of the phase evaluation, four distinct temperatures, namely 700, 750, 800, and 850 °C, were selected from the range acquired from the *in situ* XRD experiment, plus 600 and 900 °C. All other synthesis parameters remained constant: $n(Na)/n(TM) = 1/1$, $n(Ni)/n(Ti) = 9/1$, 7 l h^{-1} O_2 flow rate, and 2 K min^{-1} cooling rate. As evident from the phase fractions (table S1) from Rietveld refinement analysis of the XRD data shown in figure 2, there is an obvious trend. As the temperature increases from 600 °C to 800 °C, the phase purity of NNTO increases from 79.5 to 98.5 wt.% while the fractions of the NNO and NiO impurities decrease. This is highlighted by the red dashed rectangle in figure 2. At temperatures above 800 °C, the intensity of the NNTO (104) reflection diminishes while that of the NiO (002) and NNO (111)/(20−2) reflections increases. By 900 °C, NNTO largely decomposes into NNO and NiO, which is consistent with the *in situ* XRD results.

Next, SEM images were collected from the different samples to examine the particle morphology (figures 3(a)−(e)). The flower-shaped structure of $Na_xTi_yO_z$ was observed on the surface of the secondary particles in figures 3(a) and (b), which is likely due to incomplete reaction at calcination temperatures $\leqslant$750 °C. To gain a better understanding of the structure of the samples prepared at a lower temperature and their elemental distribution, STEM and EDS measurements were conducted on NNTO obtained at 700 °C. EDS mapping (figure S3(a)) indicated a uniform distribution of Ni. In contrast, the Na and Ti signals revealed signs of inhomogeneities, which agrees with the presence of $Na_xTi_yO_z$ as an impurity phase. The latter apparently segregates on the surface of the secondary particles at lower calcination temperatures. HAADF images at different magnifications of a FIB-prepared specimen are shown in figures S3(b)−(d). Some minor variations in contrast are clearly visible, which may be indicative of local non-uniformities. However, the high-resolution image in figure S3(d) indicates that a well-layered structure is already present at 700 °C.

A smooth particle surface was observed upon reaching 800 °C (figure 3(c)). EDS mapping confirmed the uniform distribution of Ni, Na, and Ti on different length scales (figures 4(a) and S4), while cross-sectional STEM imaging (figures 4(b)−(d)) revealed a well-defined secondary/primary particle morphology and a distinct layered structure. This demonstrates that the diffusion kinetics of titanium and sodium, which is correlated to the reaction between NNO and $Na_xTi_yO_z$, is enhanced as the temperature rises from 700 °C to 800 °C. It should be noted that an uneven distribution of Na was observed in a few secondary particles (figure S(5)), which is due to sodium loss during the solid-state reaction (see discussion below). The latter leads to the formation of Na-deficient NNTO, along with trace amounts of NiO impurities (table S1). With further temperature increase beyond 800 °C, NNTO seems to first sinter into larger particles (figure 3(d)) and then to decompose into NiO and NNO, which helps explain the ill-defined particle morphology seen in figure 3(e) [8, 24–26, 31, 32, 37].

Since the NNTO samples obtained at 700, 750 and 800 °C had a higher overall purity, their electrochemical behavior was further investigated. To this end, all three materials were incorporated into electrodes and cycled against Na metal

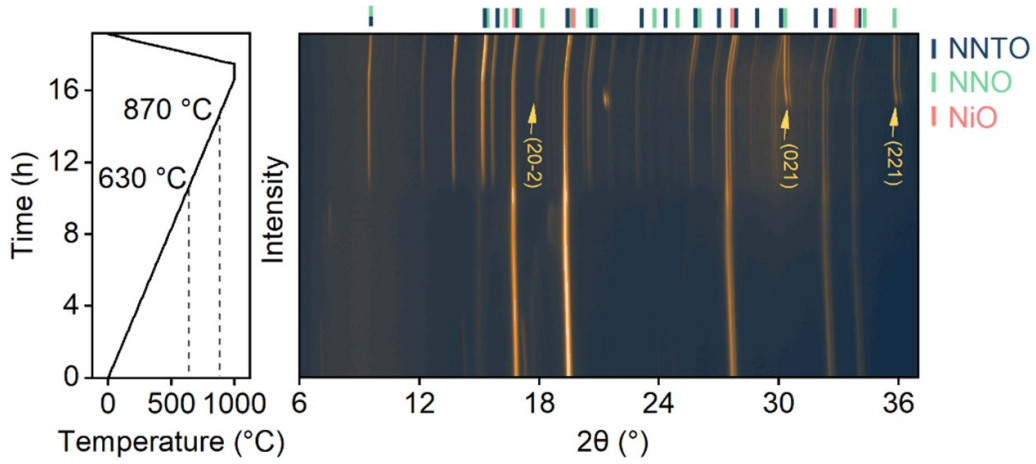

Figure 1. Contour plot of *in situ* XRD data collected from the pre-heated NNTO mixture during calcination under O_2 atmosphere.

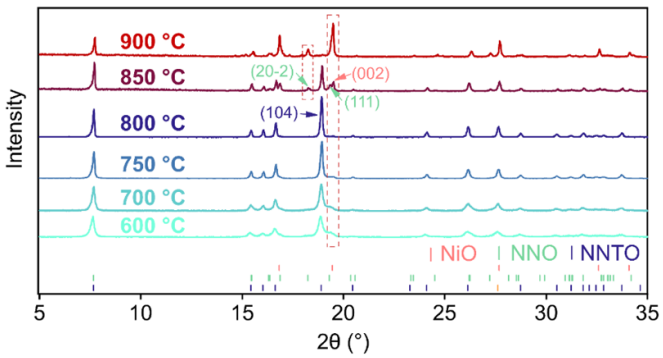

Figure 2. XRD patterns of NNTO prepared at different calcination temperatures.

in the potential range between 2.0 and 4.2 V vs. Na^+/Na at C-rates ranging from C/30 to 1C. As evident from the voltage profiles shown in figures S6(a)−(c), they exhibit promising initial Coulomb efficiencies of 91% (700 °C), 93% (750 °C), and 94% (800 °C). This is indicative of improved Na^+ diffusivity in NNTO as compared to NNO (first-cycle Coulomb efficiency of 69%) and $NaNi_{0.5}Ti_{0.5}O_2$ (first-cycle Coulomb efficiency of 74%). By comparing the cycling performance, NNTO prepared at 800 °C, which also had the highest purity, was found to exhibit the least polarization, as well as the best stability and rate capability (figures 3(f) and S6(d)−(f)). Therefore, the calcination temperature of 800 °C was applied throughout the rest of this study.

In addition to the calcination temperature, the molar Na/TM ratio can also strongly affect the material's performance. For this reason, three different ratios, namely 1, 1.025, and 1.05, which should theoretically produce Na-deficient, stoichiometric, and Na-excess NNTO, respectively, were explored in this study. As evident from the XRD patterns in figure 5(a) and the phase fractions given in table S2, all three ratios yield high-purity NNTO (>97 wt.%). ICP-OES (table S3) revealed an average sodium loss in the range of 1−3 mol.% for the different samples, which agrees with reported findings [50, 51]. Notably, it seems that the formation of NNO becomes more energetically favorable with increasing sodium excess.

SEM was then applied to visualize the influence of the molar Na/TM ratio on the NNTO properties. The images in figures 5(b) and (c) (see also figure 3(c)), as well as the particle size distributions acquired from the SEM data (figure 5(d)), clearly indicate the growth of primary particles from d_{50} = 355 nm for n(Na)/n(TM) = 1.0 to 516 nm for 1.05. This finding can be ascribed to the excess NaOH serving as a flux during calcination. Note that the primary particle size usually has a profound effect on the cycling performance. Accordingly, electrochemical tests were performed under the same conditions to verify this hypothesis. The different voltage profiles for the initial cycle (figures S6(c) and S7(a) and (b)) were similar—the materials delivered comparable specific capacities at C/30. However, the discharge capacity of NNTO prepared with molar Na/TM ratios of 1.025 and 1.05 decreased strongly with increasing C-rate (figure 5(e)), thus pointing toward slower diffusion kinetics with increasing primary particle size. This is in agreement with the higher polarization apparent from the dq/dV curves in figures S7(c) and (d) compared to figure S6(f). The superior performance of NNTO prepared with n(Na)/n(TM) = 1.0 could also be attributed to the slight sodium deficiency, as vacancy sites likely facilitate sodium transport [38]. Regardless, the ratio was set to 1 hereafter.

In addition to the previously mentioned calcination temperature and the molar Na/TM ratio, the cooling rate has varying effects on the performance and morphology of layered oxides too. Here, we have investigated NNTO by using three different cooling rates, namely 0.5 K min^{-1}, 2 K min^{-1}, and quenching in O_2 atmosphere (see Experimental section for more details). All other synthesis parameters remained constant: n(Na)/n(TM) = 1/1, n(Ni)/n(Ti) = 9/1, 7 l h^{-1} O_2 flow

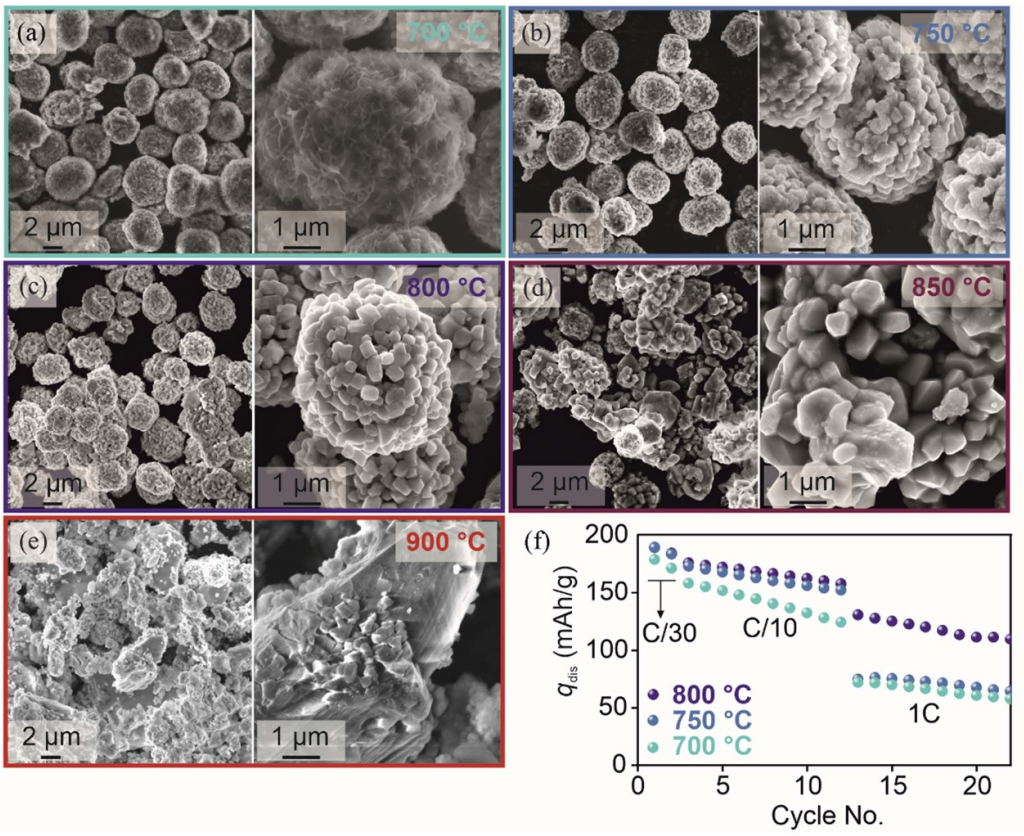

Figure 3. (a)−(e) Low- and high-magnification SEM images of NNTO prepared at different calcination temperatures. (f) Cycling performance of samples obtained at 700, 750, and 800 °C.

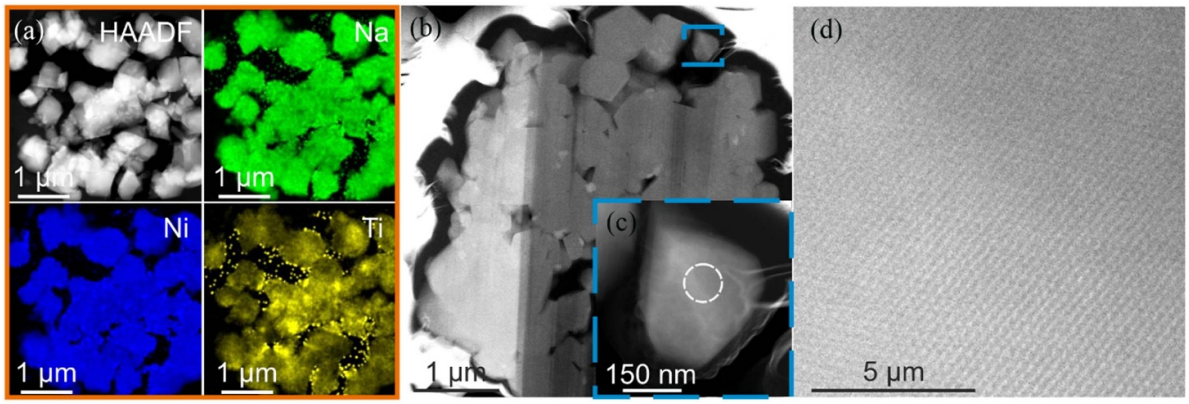

Figure 4. (a) STEM-EDS mapping of NNTO (800 °C). The random dots in the Ti map are artifacts. (b), (c) Low- and high-magnification cross-sectional HAADF STEM images of a FIB-prepared NNTO (800 °C) particle. (d) High-resolution image of the area indicated by the white dashed circle in (c).

rate, and 800 °C calcination temperature. XRD analysis was first conducted on the obtained samples. Figure 6(a) and table S4 demonstrate that only NNTO prepared at a cooling rate of 0.5 K min^{-1} exhibits relatively lower purity (96.1 wt.%). This can be attributed to the longer annealing time caused by the slower cooling, which apparently leads to partial decomposition of NNTO and further induces growth and sintering of the primary particles (figure 6(b)). The subsequent electrochemical testing (figures 6(e) and (f)) indicated that the larger primary particles, resulting from slow cooling, negatively affect the rate capability. Notably, despite the comparable primary particle size between the quenched and 2 K min^{-1} samples (figures 6(d) and 5(d)), with d_{50} = 403 and 355 nm, respectively, the quenched NNTO experienced much stronger capacity fading. This discrepancy seems to be due to the presence of cracks (see magnified SEM image in figure 6(c)) on the primary particle level produced by quenching, which apparently leads to more serious degradation during cycling [41]. Therefore, a cooling rate of 2 K min^{-1} was maintained in the following.

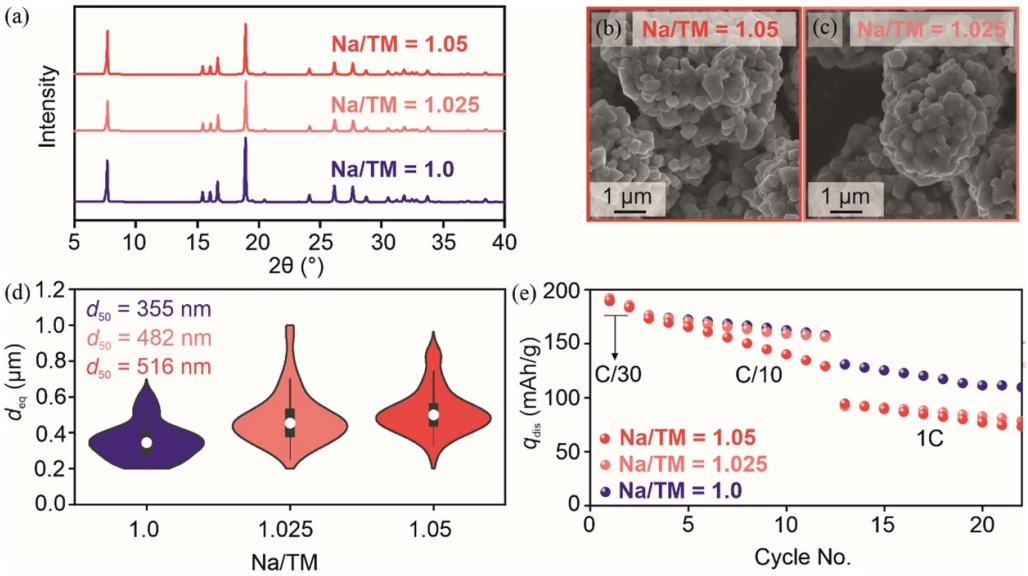

Figure 5. (a) XRD patterns, (b), (c) SEM images, (d) primary particle size distributions, and (e) cycling performance of NNTO prepared with different molar Na/TM ratios.

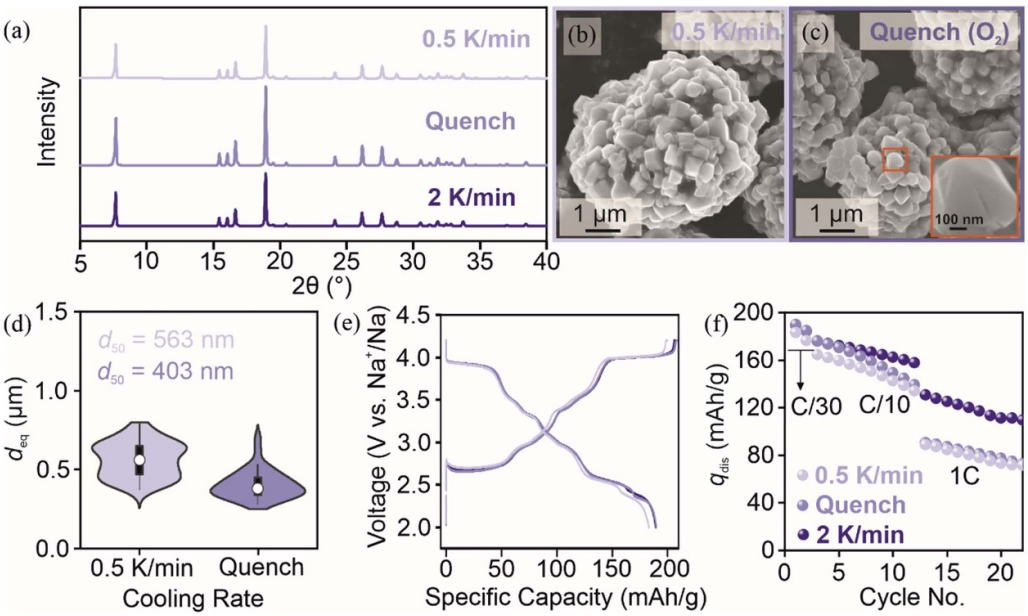

Figure 6. (a) XRD patterns, (b), (c) SEM images, (d) primary particle size distributions, (e) first-cycle voltage profiles, and (f) cycling performance of NNTO prepared with different cooling rates.

To explore the effect that the flow rate of O_2 has on the morphology and purity of NNTO, calcinations were performed at high (7 l h^{-1}) and low rates (1.4 l h^{-1}). XRD analysis (figure 7(a)) revealed that the phase fraction of NiO decreases while that of NNTO increases with increasing rate (table S5). This observation indicates that sufficient O_2 supply facilitates the oxidation of Ni^{2+} to Ni^{3+} to generate the layered structure. Figure 7(b) presents SEM images of NNTO prepared with the lower O_2 flow rate. Notably, the primary particle size was found to be markedly larger in this case (SEM images at different magnifications of NNTO prepared with the higher O_2 flow rate are shown in figure 3(c)). This can potentially be attributed to the following reasons. In the synthesis of NNO, particle sizes of $d_{50} \approx 1.4$ and 3.6 μm are achieved at 600 and 700 °C, respectively [23]. However, the polycrystalline morphology of the $Ni(OH)_2$ precursor (figure S1(a)) used here was retained by introducing Ti^{4+} into the NNO, which demonstrates the profound effect that titanium substitution has on the primary particle size in NNTO. When the O_2 flow rate is reduced, the relatively slower NiO oxidation can impede the reaction of the precursor particles with the titanium source. Consequently, these incompletely reacted precursor particles undergo growth (to larger NNO grains) and are then slowly sodiated by the $Na_xTi_yO_z$ present on the surface, resulting in

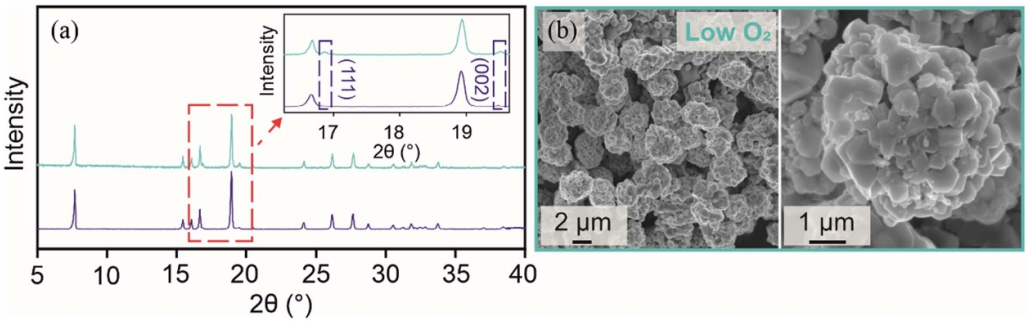

Figure 7. (a) XRD patterns of NNTO prepared with different O_2 flow rates of 1.4 l h^{-1} (cyan) and 7 l h^{-1} (purple). (b) SEM images at different magnifications of the 1.4 l h^{-1} sample.

the formation of bigger NNTO primary particles. However, local cooling effects with increasing flow rate cannot be ruled out. In agreement with the phase purity and primary particle size, the electrochemical testing (figure S(8)) confirmed that NNTO prepared with the higher O_2 flow rate delivers higher specific capacities, independent of the C-rate.

Furthermore, experiments were performed to examine the effect of varying molar Ni/Ti ratios on the material's performance. For a titanium content of 5 mol.%, the $R-3m$ phase fraction from Rietveld refinement analysis (table S6) was found to be only 46.6 wt.%, while the $C2/m$ fraction was 49.4 wt%. We attribute the higher proportion of residual NNO to an insufficient titanium content for proper suppression of the Jahn–Teller distortion in NNO. Likewise, we attempted the synthesis with 15 and 20 mol.% titanium. However, under the same calcination conditions, the fraction of $R-3m$ phase decreased with increasing degree of substitution. Despite applying the optimized preparation route for NNTO, as well as literature known ones for synthesizing $NaNi_{0.5}Ti_{0.5}O_2$, we were not able to obtain phase-pure materials for the intermediate stoichiometries [31, 37]. The SEM images presented in figures S9(a)–(c), especially those in figure S9(a), suggest that the morphology of the primary particles resembles that of NNO [23], albeit they are smaller in size due to the presence of titanium, the latter preventing sintering of grains. Furthermore, as can be seen from figures S9(b) and (c), the surface of the secondary particles is increasingly covered with nanoscale particles with increasing titanium content. This might be attributed to Ti^{4+} reaching its solubility limit. However, it should be noted that for $NaNi_{0.5}Ti_{0.5}O_2$, an $R-3m$ phase fraction of 93 wt.% (7 wt.% NiO) has been reported in the literature [31, 37]. Overall, the synthesis variables were tailored using the one parameter at a time approach, yielding the following optimal conditions: n(Na)/n(TM) = 1/1, n(Ni)/n(Ti) = 9/1, 800 °C, 2 K min^{-1}, and 7 l_{oxygen} h^{-1}. The structural parameters from Rietveld analysis of NNTO prepared with these optimized conditions are given in table S7.

When compared with $NaNi_{0.5}Ti_{0.5}O_2$ and NNO, the reversible specific capacity of NNTO is greatly enhanced [25, 26, 31, 32]. However, due to the relatively larger ionic radius of Na^+, NNTO, like most O3-type cathodes in SIBs, undergoes complex phase transitions resulting from the gliding of TMO_2 slabs. This can be clearly seen from the voltage profiles and dq/dV curves shown in figures S6(c) and (f), respectively. Even though the introduction of Ti^{4+} into the Ni sites helps mitigate the phase transitions to some extent, fading issues persist.

To further investigate the charge-storage properties of NNTO, electrochemical testing was done on half-cells. To this end, NNTO was fabricated into electrodes, as described in the Experimental section, and cycled against Na metal as the counter electrode in coin cells in the potential window of 2.0–4.2 V vs. Na^+/Na. The electrolyte was a mixture of 1 M $NaClO_4$ in EC:PC:DMC (1:1:1 by vol.) with 5 vol.% FEC additive. FEC was used to enhance the reversibility of the Na^+ insertion/extraction reactions (figure S(10)) [31, 52]. For long-term cycling, initially five cycles at C/30 were performed to ensure formation of a robust cathode solid-electrolyte interphase (cSEI). Subsequently, the cells were cycled at C/2 in the following 200 cycles. It should be noted that the latter C-rate is comparatively higher and more realistic than those (C/20 or C/10) often applied in the study of other O3-type cathode materials in SIBs [31, 53]. The cycling data (figure 8(a)) revealed an average Coulomb efficiency of 99.2% at C/2 and a capacity retention of 26.4% after 200 cycles. In comparison to $NaNi_{0.5}Ti_{0.5}O_2$, which exhibits a capacity retention of only ∼53% after 50 cycles at C/5 in the potential range between 2.0 and 4.7 V, NNTO demonstrates improved stability, maintaining 64% after 50 cycles at C/2 [31]. Nevertheless, the fading of NNTO cannot be ignored. The voltage profiles and dq/dV curves in figures S11(a) and (b), respectively, indicate severe impedance buildup with cycling. Rate performance testing was also conducted (figure 8(b)), revealing distinct capacity decay with increasing C-rate. This can be attributed to the diffusion resistance in O3-type cathodes, which is amplified with increasing current density, leading to severe polarization. However, NNTO still managed to deliver a specific discharge capacity of 89 mAh g^{-1} at 2C. Upon reducing the C-rate back to C/30, the capacity failed to reach that achieved in the initial cycles (∼190 mAh g^{-1}). Compared to the extensively studied $NaNi_{0.5}Ti_{0.5}O_2$ [31], NNTO exhibits superior rate capability. This highlights that the inclusion of Ti^{4+} in NNTO improves the sodium transport properties.

To determine the oxidation state of nickel in the pristine and cycled states, representative NNTO and NNO cathodes

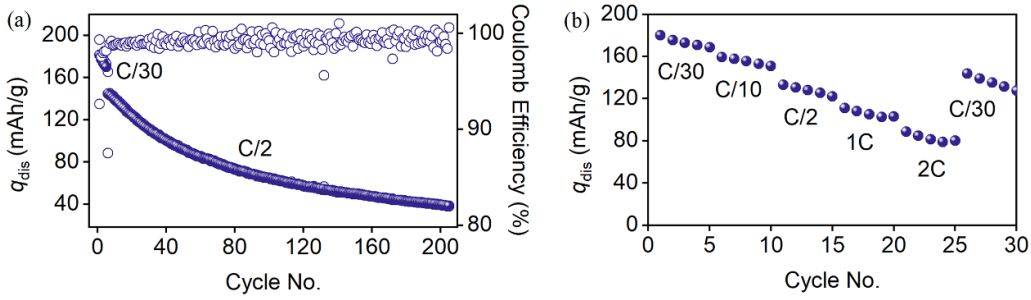

Figure 8. (a) Long-term cycling performance of NNTO in coin half-cells and (b) corresponding rate capability.

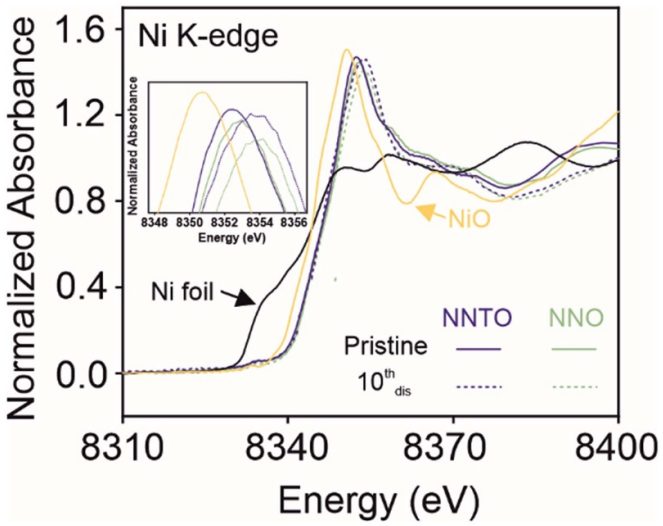

Figure 9. *Ex situ* XANES spectra at the Ni K-edge of NNTO and NNO in the pristine and discharged states (after 10 cycles).

were probed using XAS. We note that due to the limited resolution of the laboratory spectrometer used in this study, accurate testing of the oxidation state of the titanium substituent was not possible. To ensure comparability of the electrodes across various states, both NNTO and NNO were subject to electrochemical testing under the same conditions (figure S(12)). Subsequently, XAS measurements were conducted on both the pristine electrodes and those collected in the discharged state after 10 cycles. As can be seen from figure 9, the Ni K-edge of pristine NNTO lies between that of NNO and NiO, indicating the coexistence of Ni^{2+} and Ni^{3+}, as expected from the titanium substitution. After 10 cycles, because of localized structural alterations, both NNTO and NNO exhibit varying degrees of rightward shifts at the Ni K-edge. However, the energy position of NNO was about 1 eV higher than that of NNTO, indicating that NNTO has a better structural stability.

For a more detailed understanding of the structural changes occurring in NNTO during cycling, *operando* XRD was conducted on the cathodes. The contour plot in figure 10(a) reveals four reversible phase transitions. Due to the low intensity (laboratory diffractometer), continuous refinement was not possible. Therefore, individual XRD patterns were refined to describe the structural evolution. As shown in figure S(13), the Ni^{2+} ions undergo oxidation to Ni^{3+} upon Na^+ extraction, which enhances the Jahn–Teller distortion and leads to the emergence of monoclinic distortion and formation of the O'3 phase. The most prominent feature was a splitting of the (104) reflection into (20−2) and (111) for O'3. However, the (20−2) reflection was barely visible (low intensity). With further desodiation, the repulsion within the oxygen layers increases, causing gliding of the TMO_2 slabs and formation of the P3 phase. The most noticeable change was a significant enhancement of the (105), (102), (006), and (003) reflections [7]. As the sodium content depleted further, P3 transitioned toward O"3, causing less lattice distortion. The latter is evident from the decrease in *a*/*b* value from O'3 (1.86) to O"3 (1.83) [25]. Nevertheless, the cubic volume of O"3 is slight larger than that of P3 (table S8). Similar results have been reported for other (charged) Ni-rich O3-type layered oxides in SIBs, such as O'3-$NaNiO_2$ and O3-$NaNi_{0.5}Co_{0.5}O_2$ [25, 53–57]. With progressing desodiation, the Ni^{3+} ions undergo further oxidation to Ni^{4+}, accompanied by the formation of the O1 phase. The hypothesis is that O1 is thermodynamically more stable at high states of charge, similar to the O3-O1 transition occurring in $LiCoO_2$ (LCO) [58]. The different transitions (based on the discharge data in table S8) are indicated in the dq/dV curve for the second cycle in figure S(14), aiming at providing a more intuitive understanding of the phase changes. Due to significant overpotentials in the initial charge cycle, an accurate comparison is not feasible. It should be noted that the peaks at about 3.1, 3.4, and 3.5 V (figure S(14)) cannot be unambiguously correlated with features in the XRD data; they can likely be attributed to Na^+/vacancy ordering or reversible reactions involving the Ni^{2+}–Ni^{3+} and/or Ni^{3+}–Ni^{4+} redox couples, with the former potentially stabilizing the monoclinic O"3 phase and facilitating its formation [56, 59–62].

The structural parameters from Rietveld refinements of the individual XRD patterns are given in table S8. All unit-cell volumes were translated into values analogous to the primitive cubic cell for easier comparison between different phases. As can be seen, prior to the formation of the O1 phase, the volume changes are minor, irrespective of the transitions from O3 → O'3 → P3 → O"3 (figure 10(b)). However, upon O1 formation at potentials above 4.0 V vs. Na^+/Na (equivalent to ∼80% state of charge), the volume collapses to about 70% of the initial O3 volume, eventually resulting in the formation of cracks (figures 10(c) and (d)) and leading to mechanical

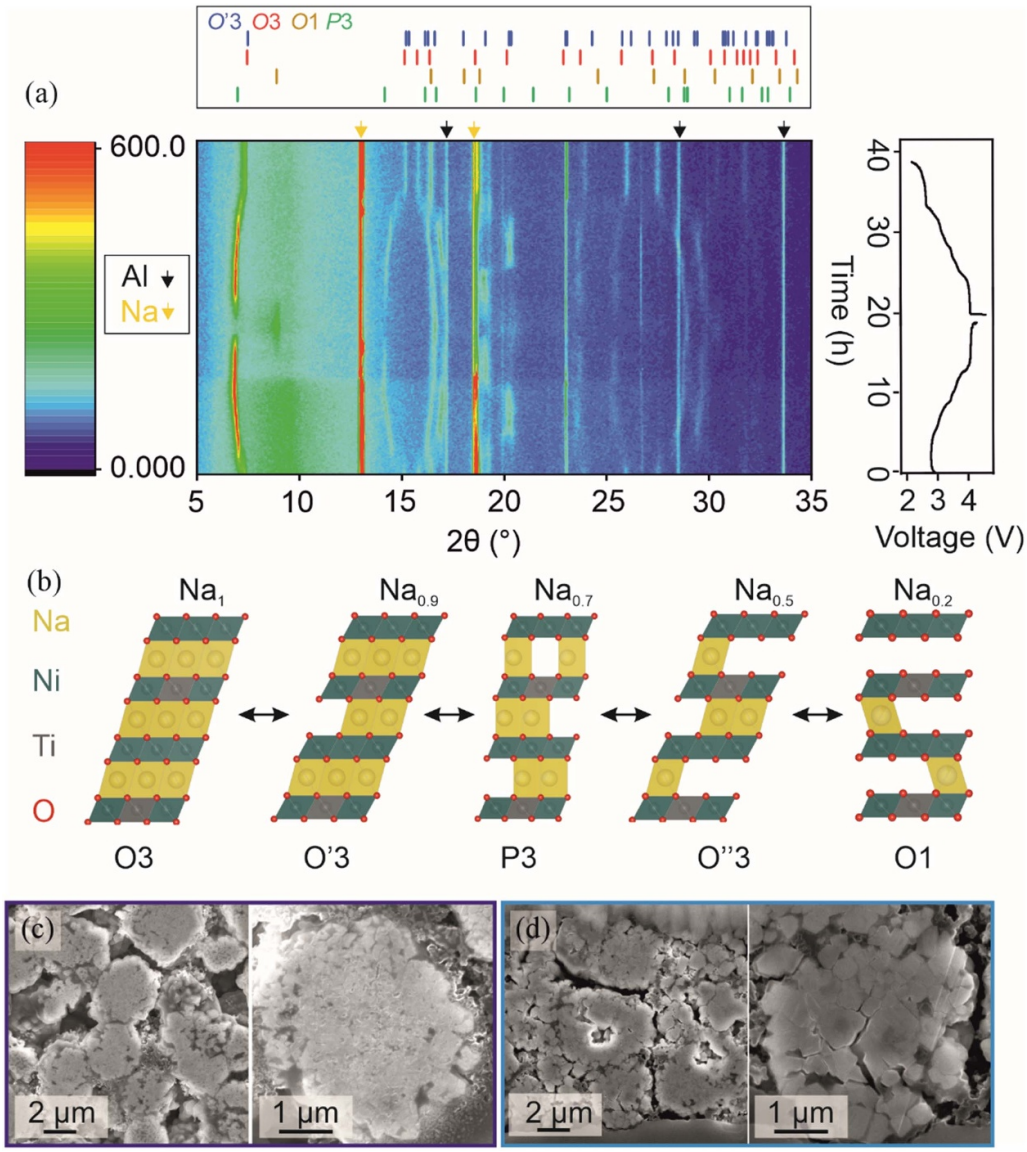

Figure 10. (a) 2D contour plot of *operando* XRD data collected during the first cycle at C/10 rate. (b) Illustration of crystal structures for O3, O'3, P3, O"3, and O1. Cross-sectional SEM images of NNTO (c) in the pristine state and (d) after 200 cycles.

degradation. A similar fading behavior has been observed for the O3-type $NaNi_{0.5}Mn_{0.5}O_2$ [36]. Notably, although the P3 phase is in a Na-deficient state, its *c* parameter was found to not deviate much from that of the initial O3 phase. This can be explained by weakening of the oxygen–oxygen shielding effect upon Na^+ extraction [63].

To gain further insight into crack formation during cycling of NNTO, *operando* AE as a non-destructive technique was employed. AE is widely used for monitoring the fatigue and mechanical damage of construction materials [64]. Regarding batteries, AE has been employed both to monitor cell health and predict cycle life, and as a characterization tool for individual electrodes [65–67]. While (bulk) phase evolution can be studied via XRD, information about microscopic structural changes, such as particle fracture, are not easily obtained in *operando* mode [68]. By monitoring the AE of NNTO, particle cracking can be examined. In general, AE directly detects the generation and propagation of cracks, thereby indirectly providing information about structural changes on the material and/or electrode level. Nevertheless, other acoustically active processes can be monitored as well, such as SEI formation [46, 64, 68, 69]. As shown in figures 11(a) and (b), acoustic activity accumulated early in the initial cycle, due to formation of the cSEI [68, 70–73]. This has also been found for LCO and LNO cathodes [68, 70]. Near the end of charge and in subsequent cycles, the majority of acoustic activity was detected at potentials associated with particle fracture due to phase transitions and the corresponding unit-cell volume changes during desodiation [68, 70, 71, 74–76]. The number of new hits per cycle gradually decreased, which is reflected in the hit density shown in figure 11(b) and highlighted for the later cycles in figure S15(a). A similar observation of AE being closely related to particle fracture has recently been reported for a P2-type SIB CAM [46].

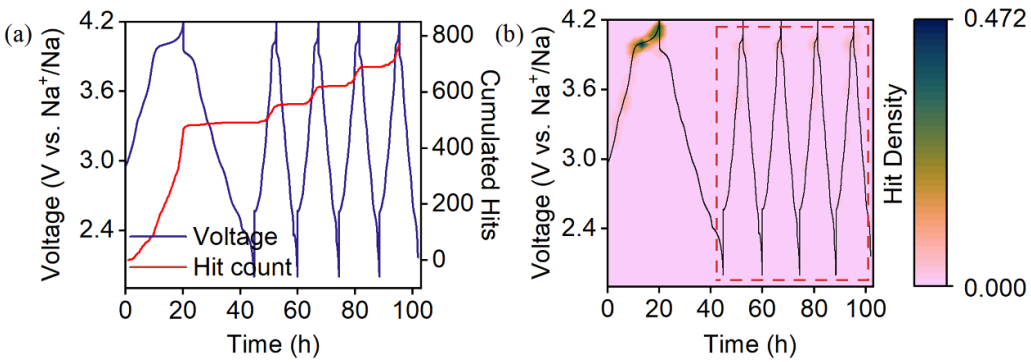

Figure 11. (a) Voltage profiles for the first five cycles (at C/30 rate followed by C/10 cycling) and corresponding cumulated hits. (b) Contour plot of acoustic activity (hit density) as a function of time and potential.

Since the AE is concentrated in the phase-transition regions, dq/dV curves of the first two cycles are displayed in figures S15(b) and (c). In the beginning of the initial cycle, which corresponds to the (acoustically active) cSEI formation stage, the acoustic behavior associated with phase transitions was relatively weak, but strong activity caused by the O"3-O1 transition at about 4.0 V vs. Na^+/Na was clearly observed. In the second cycle, two distinct peaks, centered around 3.5 V, led to acoustic activity. A possible reason might be Na^+/vacancy ordering, leading to a reduction in Jahn–Teller distortion and further resulting in strain concentration, plastic deformation, and/or intragranular cracking [53]. While Jahn–Teller distortion can be observed by XRD, the latter effects may only be detected in real-time by AE or advanced electron microscopy techniques. However, other peaks in the dq/dV curves were not associated with distinct acoustic behavior. Overall, the volume collapse at high potentials can be correlated with specific AE signals, strongly suggesting crack formation. Therefore, it seems that chemo-mechanical degradation is one of the main factors contributing to the NNTO fading.

Finally, *in situ* DEMS measurements were performed to study the gassing behavior of NNTO. Figures 12(a)−(d) illustrates the relationship between voltage profile and gas evolution rate and total amount of the three species detected, namely hydrogen (H_2, $m/z = 2$), oxygen (O_2, $m/z = 32$), and carbon dioxide (CO_2, $m/z = 44$). The evolution of these gases can be seen in analogy to their generation in LIBs. CO_2 originates from the chemical oxidation of electrolyte associated with the release of lattice oxygen or from electrochemical oxidation of the electrolyte (or, mainly during the initial cycle, from surface carbonates) [77–82]. In LIBs, the O_2 released from layered oxide cathode materials is reactive oxygen and is seldom directly detected in the form of molecular oxygen. Instead, it is indirectly detected in the form of the electrolyte oxidation product CO_2 [83, 84]. However, small amounts of O_2 were observed in this study. H_2 is initially generated through the reduction of trace water at the anode. Its release at higher potentials is typically attributed to the formation of protic species as secondary products, stemming from oxidation reactions involving the electrolyte, at the cathode. These species then migrate to the anode, where they undergo reduction processes under the release of H_2 (figure 12(b)) [81, 82, 85]. In the first cycle, a small amount of O_2 (∼2.9 μmol g^{-1}) evolved (figure 12(c)), which can be attributed to NNTO undergoing oxygen redox activation, as known for O3-type layered oxides containing redox-inactive transition metals [86, 87]. This in turn can lead to anion oxidation at higher potentials, resulting partially in irreversible O_2 evolution [82, 87, 88]. The main evolved gas was CO_2 (figure 12(d)), with the highest rate at about 4.0 V vs. Na^+/Na. Generally, residual carbonates can explain much of the CO_2 evolution in the initial cycle [78]. However, no carbonate vibrational bands were detected by Fourier-transform infrared spectroscopy (figure S(16)), indicating a largely carbonate-free surface of the NNTO secondary particles. Because the H_2 evolution exhibited a similar behavior (figure 12(b)), we attribute the generation of H_2 and a major portion of CO_2 at 4.0 V to the reaction between released lattice oxygen and electrolyte. A smaller portion of CO_2, explaining the gas evolution shoulder at 4.2 V, may be attributed to the decomposition of trace carbonates and/or electrochemical oxidation of the electrolyte, which however is commonly observed only at potentials above 4.7 V vs. Li^+/Li (equivalent to ∼4.4 V vs. Na^+/Na), and thus considered less likely [82]. In the second cycle, due to the formation of the cSEI and an oxygen-depleted surface, the gas generated by chemical oxidation of electrolyte significantly decreased. Yet, small amounts of H_2 and CO_2 were observed, implying the persistence of lattice oxygen loss and subsequent electrolyte degradation. In conclusion, the gassing behavior infers that irreversible oxidation of lattice oxygen is, next to the phase transitions and resulting particle fracture, another underlying mechanism of the continuous degradation of NNTO.

In addressing the two degradation mechanisms mentioned above, a preliminary optimization was performed. For mitigating chemo-mechanical degradation induced by continuous cracking, an Al_2O_3 coating was applied to the NNTO secondary particles [89–92]. The purpose was to prevent adverse side reactions from occurring between newly formed (reactive) interfaces and electrolyte. As shown in figure S(17), the Al_2O_3 coating indeed helps stabilize the NNTO surface, improving the cycling stability, although some degradation remains. In the future, dopants may be employed, along with protective coatings. This approach is expected to not only alleviate the volume collapse of NNTO at high potentials, but also to

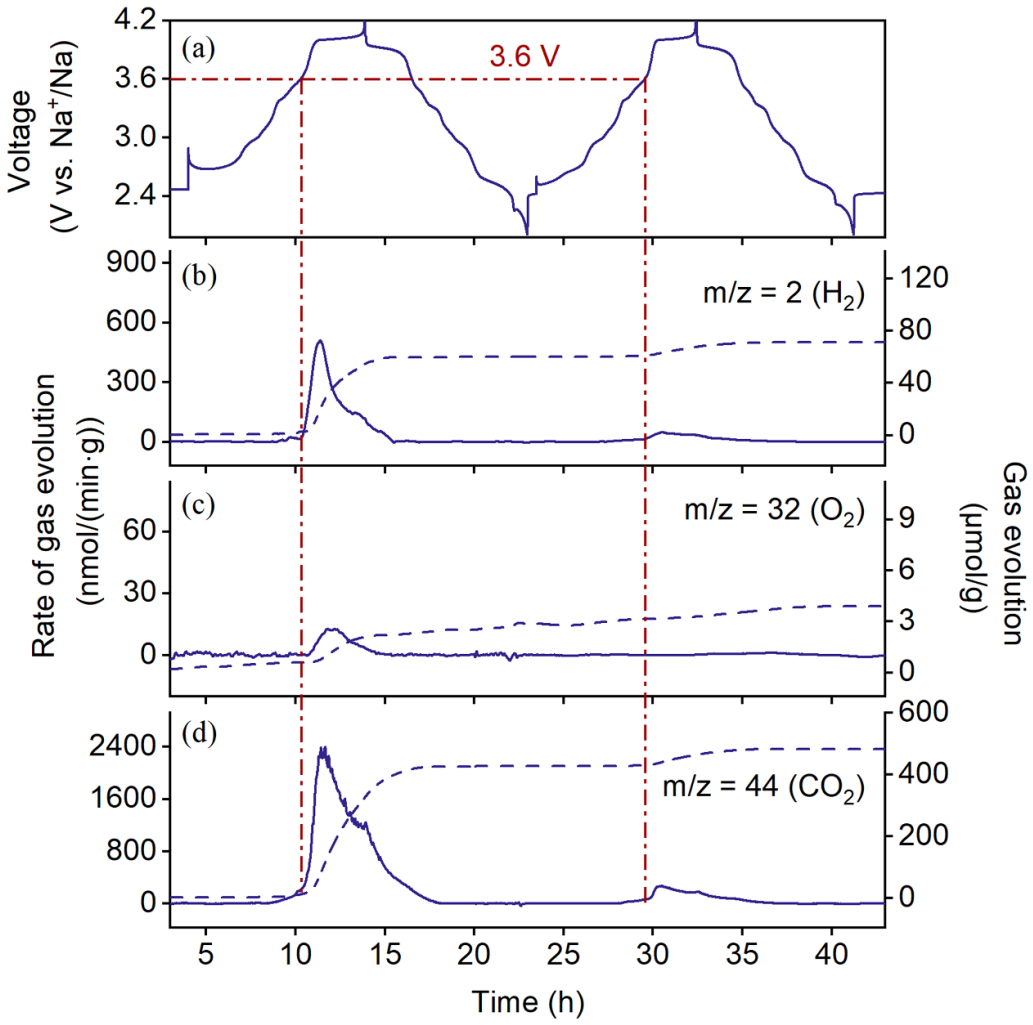

Figure 12. (a) Voltage profiles at C/10 rate and corresponding time-resolved evolution rates (left *y*-axis) and cumulative amounts (right *y*-axis) of (b) H_2, (c) O_2, and (d) CO_2 measured by DEMS.

suppress lattice oxygen loss to ultimately enhancing the overall cycling performance.

4. Conclusions

In summary, in the present work, we have reported about $NaNi_{0.9}Ti_{0.1}O_2$ (NNTO), which is superior to $NaNiO_2$ and $NaNi_{0.5}Ti_{0.5}O_2$ when used as a cathode material in sodium-ion cells. By systematic exploration of the synthesis conditions, high-purity NNTO was prepared through a solid-state route. The material is capable of delivering a reversible specific capacity of $q_{dis} \approx 190$ mAh g^{-1} in the electrochemical window of 2.0−4.2 V vs. Na^+/Na at an average operating potential of 3.2 V. Compared to $NaNiO_2$ and $NaNi_{0.5}Ti_{0.5}O_2$, NNTO demonstrates increased cycling stability even at higher C-rates (maintaining ∼64% of the capacity after 50 cycles at C/2). However, significant fading is still observed upon long-term cycling. Through *operando* XRD, we found that NNTO undergoes an O"3-O1 phase transition at around 4.0 V, causing a ∼30% volume collapse and resulting in crack initiation and propagation during battery operation. This observation was verified through *post mortem* SEM imaging and *operando* AE measurements. Furthermore, *in situ* gas analysis via DEMS revealed irreversible lattice oxygen loss, contributing to structural instability and fading. To address these degradation mechanisms, we have implemented an alumina surface coating, and intend to introduce dopants into the Na sites [93], or further to the transition metal sites of NNTO, to mitigate the volume variation at high potentials.

5. Future perspectives

The rapid advancement of LIBs has significantly propelled the electric and hybrid vehicle industry in recent years. SIBs, as a promising alternative to LIBs, are particularly suitable for large-scale electrochemical energy storage, due to their lower cost and the abundant availability of raw materials. However, recent research on layered oxide cathodes has revealed that favorable operating potentials and high theoretical specific capacities make SIBs also viable for high-performance applications. Among the existing layered oxides, sodium-rich O3-type materials generally exhibit a higher

theoretical specific capacity than sodium-deficient P2-type materials, making the former more promising for practical application. Nonetheless, the multiple phase transitions and Jahn–Teller distortion associated with O3-type structures can severely affect the cycling performance and stability. Doping transition metal sites with tetravalent metal species (such as Ti^{4+}) has been shown to effectively mitigate some of the issues. Despite these advances, further investigation into the material's stability/reactivity (bulk/surface) at high potentials is required to fully realize the potential of this promising class of cathode materials.

Acknowledgments

This study was supported by BASF SE. The authors thank Dr Thomas Bergfeldt (KIT) and Dr Philipp Müller (BASF SE) and their teams for collecting the ICP-OES and TEM data, respectively. J J and M F acknowledges funding by the German Research Foundation (DFG) under project ID 390874152 (POLiS Cluster of Excellence). This work contributes to the research performed at CELEST (Center for Electrochemical Energy Storage Ulm-Karlsruhe).

Conflict of interest

The authors declare no conflict of interest.

ORCID iD

Torsten Brezesinski https://orcid.org/0000-0002-4336-263X

References

[1] Manthiram A 2020 A reflection on lithium-ion battery cathode chemistry *Nat. Commun.* **11** 1550
[2] Chang U, Lee J T, Yun J-M, Lee B, Lee S W, Joh H-I, Eom K and Fuller T F 2019 *In situ* self-formed nanosheet MoS_3/reduced graphene oxide material showing superior performance as a lithium-ion battery cathode *ACS Nano* **13** 1490–8
[3] Yuan T *et al* 2022 A high-rate, durable cathode for sodium-ion batteries: sb-doped O3-type Ni/Mn-based layered oxides *ACS Nano* **16** 18058–70
[4] Chayambuka K, Mulder G, Danilov D L and Notten P H L 2018 Sodium-ion battery materials and electrochemical properties reviewed *Adv. Energy Mater.* **8** 1800079
[5] Gao R-M, Zheng Z-J, Wang P-F, Wang C-Y, Ye H and Cao F-F 2020 Recent advances and prospects of layered transition metal oxide cathodes for sodium-ion batteries *Energy Storage Mater.* **30** 9–26
[6] Li S, Sun Y, Pang Y, Xia S, Chen T, Sun H, Zheng S and Yuan T 2022 Recent developments of layered transition metal oxide cathodes for sodium-ion batteries toward desired high performance *Asia-Pac. J. Chem. Eng.* **17** e2762
[7] Wang P-F, Yao H-R, Liu X-Y, Zhang J-N, Gu L, Yu X-Q, Yin Y-X and Guo Y-G 2017 Ti-substituted $NaNi_{0.5}Mn_{0.5-x}Ti_xO_2$ cathodes with reversible O3-P3 phase transition for high-performance sodium-ion batteries *Adv. Mater.* **29** 1700210
[8] Guo S, Yu H, Liu P, Ren Y, Zhang T, Chen M, Ishida M and Zhou H 2015 High-performance symmetric sodium-ion batteries using a new, bipolar O3-type material, $Na_{0.8}Ni_{0.4}Ti_{0.6}O_2$ *Energy Environ. Sci.* **8** 1237–44
[9] Wang P-F, You Y, Yin Y-X, Wang Y-S, Wan L-J, Gu L and Guo Y-G 2016 Suppressing the P2-O2 phase transition of $Na_{0.67}Mn_{0.67}Ni_{0.33}O_2$ by magnesium substitution for improved sodium-ion batteries *Angew. Chem., Int. Ed.* **128** 7571–5
[10] Han M H, Gonzalo E, Singh G and Rojo T 2015 A comprehensive review of sodium layered oxides: powerful cathodes for Na-ion batteries *Energy Environ. Sci.* **8** 81–102
[11] Guo S, Liu P, Yu H, Zhu Y, Chen M, Ishida M and Zhou H 2015 A layered P2- and O3-type composite as a high-energy cathode for rechargeable sodium-ion batteries *Angew. Chem., Int. Ed.* **54** 5894–9
[12] Xie Y *et al* 2021 Role of lithium doping in P2-$Na_{0.67}Ni_{0.33}Mn_{0.67}O_2$ for sodium-ion batteries *Chem. Mater.* **33** 4445–55
[13] Delmas C, Fouassier C and Hagenmuller P 1980 Structural classification and properties of the layered oxides *Physica* B+C **99** 81–85
[14] Delmas C, Braconnier J-J, Fouassier C and Hagenmuller P 1981 Electrochemical intercalation of sodium in Na_xCoO_2 bronzes *Solid State Ion.* **3–4** 165–9
[15] Nitta N, Wu F, Lee J T and Yushin G 2015 Li-ion battery materials: present and future *Mater. Today* **18** 252–64
[16] Blomgren G E 2017 The development and future of lithium ion batteries *J. Electrochem. Soc.* **164** A5019–25
[17] Noh H-J, Youn S, Yoon C S and Sun Y-K 2013 Comparison of the structural and electrochemical properties of layered $Li[Ni_xCo_yMn_z]O_2$ (x=1/3, 0.5,0.6, 0.7, 0.8 and 0.85) cathode material for lithium-ion batteries *J. Power Sources* **233** 121–30
[18] Kim J-H, Ryu H-H, Kim S J, Yoon C S and Sun Y-K 2019 Degradation mechanism of highly Ni-rich $Li[Ni_xCo_yMn_{1-x-y}]O_2$ cathodes with $x > 0.9$ *ACS Appl. Mater. Interfaces* **11** 30936–42
[19] Bianchini M, Roca-Ayats M, Hartmann P, Brezesinski T and Janek J 2019 There and back again-the journey of $LiNiO_2$ as a cathode active material *Angew. Chem., Int. Ed.* **58** 10434–58
[20] Li W, Reimers J N and Dahn J R 1992 Crystal structure of $Li_xNi_{2-x}O_2$ and a lattice-gas model for the order-disorder transition *Phys. Rev.* B **46** 3236–46
[21] Reimers J N, Li W and Dahn J R 1993 Short-range cation ordering in $Li_xNi_{2-x}O_2$ *Phys. Rev.* B **47** 8486–93
[22] Shannon R D 1976 Revised effective ionic radii and systematic studies of interatomic distances in halides and chalcogenides *Acta Crystallogr.* **32** 751–67
[23] Karger L *et al* 2023 Low-temperature ion exchange synthesis of layered $LiNiO_2$ single crystals with high ordering *Chem. Mater.* **35** 648–57
[24] Vassilaras P, Ma X, Li X and Ceder G 2013 Electrochemical properties of monoclinic $NaNiO_2$ *J. Electrochem. Soc.* **160** A207–11
[25] Han M H, Gonzalo E, Casas-Cabanas M and Rojo T 2014 Structural evolution and electrochemistry of monoclinic $NaNiO_2$ upon the first cycling process *J. Power Sources* **258** 266–71
[26] Wang L, Wang J, Zhang X, Ren Y, Zuo P, Yin G and Wang J 2017 Unravelling the origin of irreversible capacity loss in $NaNiO_2$ for high voltage sodium ion batteries *Nano Energy* **34** 215–23
[27] Kang K, Meng Y-S, Breger J, Grey C P and Ceder G 2006 Electrodes with high power and high capacity for rechargeable lithium batteries *Science* **311** 977–80

[28] Luo Y *et al* 2022 Towards Ni-rich layered oxides cathodes with low Li/Ni intermixing by mild molten-salt ion exchange for lithium-ion batteries *Nano Energy* **102** 107626

[29] Cao X, Qiao Y, Jia M, He P and Zhou H 2022 Ion-exchange: a promising strategy to design li-rich and li-excess layered cathode materials for Li-ion batteries *Adv. Energy Mater.* **12** 2003972

[30] Komaba S, Yabuuchi N, Nakayama T, Ogata A, Ishikawa T and Nakai I 2012 Study on the reversible electrode reaction of $Na_{1-x}Ni_{0.5}Mn_{0.5}O_2$ for a rechargeable sodium-ion battery *Inorg. Chem.* **51** 6211–20

[31] Yu H, Guo S, Zhu Y, Ishida M and Zhou H 2014 Novel titanium-based O3-type $NaTi_{0.5}Ni_{0.5}O_2$ as a cathode material for sodium ion batteries *Chem. Commun.* **50** 457–9

[32] Maletti S, Sarapulova A, Schökel A and Mikhailova D 2019 Operando studies on the $NaTi_{0.5}Ni_{0.5}O_2$ cathode for Na-ion batteries: elucidating titanium as a structure stabilizer *ACS Appl. Mater. Interfaces* **11** 33923–30

[33] Ma Q, Peng F, Li R, Yin S and Dai C 2016 Effect of calcination temperature on microstructure and electrochemical performance of lithium-rich layered oxide cathode materials *Mater. Sci. Eng.* **213** 123–30

[34] Manzi J, Paolone A, Palumbo O, Corona D, Massaro A, Cavaliere R, Muñoz-García A B, Trequattrini F, Pavone M and Brutti S 2021 Monoclinic and orthorhombic $NaMnO_2$ for secondary batteries: a comparative study *Energies* **14** 1230

[35] Kubota K, Miyazaki M, Kim E J, Yoshida H, Barpanda P and Komaba S 2021 Structural change induced by electrochemical sodium extraction from layered O'3-$NaMnO_2$ *J. Mater. Chem.* A **9** 26810–9

[36] Yu T-Y, Ryu H-H, Han G and Sun Y-K 2020 Understanding the capacity fading mechanisms of O3-type $Na[Ni_{0.5}Mn_{0.5}]O_2$ cathode for sodium-ion batteries *Adv. Energy Mater.* **10** 2001609

[37] Wang H, Xiao Y, Sun C, Lai C and Ai X 2015 A type of sodium-ion full-cell with a layered $NaNi_{0.5}Ti_{0.5}O_2$ cathode and a pre-sodiated hard carbon anode *RSC Adv.* **5** 106519–22

[38] Zhou D, Huang W, Zhao F and Lv X 2019 The effect of Na content on the electrochemical performance of the O3-type $Na_xFe_{0.5}Mn_{0.5}O_2$ for sodium-ion batteries *J. Mater. Sci.* **54** 7156–64

[39] Liu H *et al* 2018 Truncated octahedral high-voltage spinel $LiNi_{0.5}Mn_{1.5}O_4$ cathode materials for lithium ion batteries: positive influences of Ni/Mn disordering and oxygen vacancies *J. Electrochem. Soc.* **165** A1886–96

[40] Liu X *et al* 2020 Al and Fe-containing Mn-based layered cathode with controlled vacancies for high-rate sodium ion batteries *Nano Energy* **76** 104997

[41] Xu G-L *et al* 2022 Native lattice strain induced structural earthquake in sodium layered oxide cathodes *Nat. Commun.* **13** 436

[42] Toby B H and Von Dreele R B 2013 GSAS-II: the genesis of a modern open-source all purpose crystallography software package *J. Appl. Crystallogr.* **46** 544–9

[43] Geßwein H, Stüble P, Weber D, Binder J R and Mönig R 2022 A multipurpose laboratory diffractometer for operando powder x-ray diffraction investigations of energy materials *J. Appl. Crystallogr.* **55** 503–14

[44] Jahrman E P *et al* 2019 An improved laboratory-based x-ray absorption fine structure and x-ray emission spectrometer for analytical applications in materials chemistry research *Rev. Sci. Instrum.* **90** 024106

[45] Schweidler S, Dreyer S L, Breitung B and Brezesinski T 2021 Operando acoustic emission monitoring of degradation processes in lithium-ion batteries with a high-entropy oxide anode *Sci. Rep.* **11** 23381

[46] Dreyer S L, Zhang R, Wang J, Kondrakov A, Wang Q, Brezesinski T and Janek J 2023 The effect of configurational entropy on acoustic emission of P2-type layered oxide cathodes for sodium-ion batteries *J. Phys. Energy* **5** 035002

[47] Berkes B B, Jozwiuk A, Sommer H, Brezesinski T and Janek J 2015 Simultaneous acquisition of differential electrochemical mass spectrometry and infrared spectroscopy data for in situ characterization of gas evolution reactions in lithium-ion batteries *Electrochem. Commun.* **60** 64–69

[48] Berkes B B, Jozwiuk A, Vračar M, Sommer H, Brezesinski T and Janek J 2015 Online continuous flow differential electrochemical mass spectrometry with a realistic battery setup for high-precision, long-term cycling tests *Anal. Chem.* **87** 5878–83

[49] Rudola A, Saravanan K, Mason C W and Balaya P 2013 $Na_2Ti_3O_7$: an intercalation based anode for sodium-ion battery applications *J. Mater. Chem.* A **1** 2653–62

[50] Yuan T *et al* 2023 Moisture stable and ultrahigh-rate Ni/Mn-based sodium-ion battery cathodes via K^+ decoration *Nano Res.* **16** 6890–902

[51] Darga J and Manthiram A 2022 Facile synthesis of O3-type $NaNi_{0.5}Mn_{0.5}O_2$ single crystals with improved performance in sodium-ion batteries *ACS Appl. Mater. Interfaces* **14** 52729–37

[52] Komaba S, Ishikawa T, Yabuuchi N, Murata W, Ito A and Ohsawa Y 2011 Fluorinated ethylene carbonate as electrolyte additive for rechargeable Na batteries *ACS Appl. Mater. Interfaces* **3** 4165–8

[53] Kubota K, Fujitani N, Yoda Y, Kuroki K, Tokita Y and Komaba S 2021 Impact of Mg and Ti doping in O3 type $NaNi_{1/2}Mn_{1/2}O_2$ on reversibility and phase transition during electrochemical Na intercalation *J. Mater. Chem.* A **9** 12830–44

[54] Yabuuchi N, Kubota K, Dahbi M and Komaba S 2014 Research development on sodium-ion batteries *Chem. Rev.* **114** 11636–82

[55] Braconnier J-J, Delmas C, Fouassier C and Hagenmuller P 1980 Comportement electrochimique des phases Na_xCoO_2 *Mater. Res. Bull.* **15** 1797–804

[56] Li X, Wang Y, Wu D, Liu L, Bo S-H and Ceder G 2016 Jahn–Teller assisted Na diffusion for high performance Na ion batteries *Chem. Mater.* **28** 6575–83

[57] Vassilaras P, Kwon D-H, Dacek S T, Shi T, Seo D-H, Ceder G and Kim J C 2017 Electrochemical properties and structural evolution of O3-type layered sodium mixed transition metal oxides with trivalent nickel *J. Mater. Chem.* A **5** 4596–606

[58] Van der Ven A, Aydinol M K and Ceder G 1998 First-principles evidence for stage ordering in Li_xCoO_2 *J. Electrochem. Soc.* **145** 2149–55

[59] Kaufman J L and Van Der Ven A 2019 Na_xCoO_2 phase stability and hierarchical orderings in the O3/P3 structure family *Phys. Rev. Mater.* **3** 015402

[60] Kubota K, Asari T, Yoshida H, Yaabuuchi N, Shiiba H, Nakayama M and Komaba S 2016 Understanding the structural evolution and redox mechanism of a $NaFeO_2$–$NaCoO_2$ solid solution for sodium-ion batteries *Adv. Funct. Mater.* **26** 6047–59

[61] Yabuuchi N, Ikeuchi I, Kubota K and Komaba S 2016 Thermal stability of Na_xCrO_2 for rechargeable sodium batteries; studies by high-temperature synchrotron x-ray diffraction *ACS Appl. Mater. Interfaces* **8** 32292–9

[62] Didier C, Guignard M, Suchomel M R, Carlier D, Darriet J and Delmas C 2016 Thermally and electrochemically driven topotactical transformations in sodium layered oxides Na_xVO_2 *Chem. Mater.* **28** 1462–71

[63] Ding F-X, Rong X-H, Wang H-B, Yang Y, Hu Z-L, Dang R-B, Lu Y-X and Hu Y-S 2022 Phase transitions of Na-ion

layered oxide materials and their influence on properties *Acta Phys. Sin.* **71** 108801
[64] Enoki M, Inaba H, Mizutani Y, Nakano M and Ohtsu M 2016 Principles of the acoustic emission (AE) method and signal processing *Practical Acoustic Emission Testing* (Springer)
[65] Beganovic N and Söffker D 2019 Estimation of remaining useful lifetime of lithium-ion battery based on acoustic emission measurements *J. Energy Resour. Technol.* **141** 041901
[66] Wang K, Chen Q, Yue Y, Tang R, Wang G, Tang L and He Y 2023 Cyclic aging monitoring of lithium-ion battery based on acoustic emission *Nondestruct. Test. Eval.* **38** 480–99
[67] Zhang K, Yin J and He Y 2021 Acoustic emission detection and analysis method for health status of lithium ion batteries *Sensors* **21** 712
[68] Schweidler S, Bianchini M, Hartmann P, Brezesinski T and Janek J 2020 The sound of batteries: an operando acoustic emission study of the $LiNiO_2$ cathode in Li-ion cells *Batter. Supercaps* **3** 1021–7
[69] Majasan J O, Robinson J B, Owen R E, Maier M, Radhakrishnan A N P, Pham M, Tranter T G, Zhang Y, Shearing P R and Brett D J L 2021 Recent advances in acoustic diagnostics for electrochemical power systems *J. Phys. Energy* **3** 032011
[70] Choe C-Y, Jung W-S and Byeon J-W 2015 Damage evaluation in lithium cobalt oxide/carbon electrodes of secondary battery by acoustic emission monitoring *Mater. Trans.* **56** 269–73
[71] Schweidler S, Dreyer S L, Breitung B and Brezesinski T 2022 Acoustic emission monitoring of high-entropy oxyfluoride rock-salt cathodes during battery operation *Coatings* **12** 402
[72] Tranchot A, Etiemble A, Thivel P-X, Idrissi H and Roué L 2015 In-situ acoustic emission study of Si-based electrodes for Li-ion batteries *J. Power Sources* **279** 259–66
[73] Matsuo T, Uchida M and Cho H 2011 Development of acoustic emission clustering method to detect degradation of lithium ion batteries *J. Solid Mech. Mater. Eng.* **5** 678–89
[74] Kircheva N, Genies S, Chabrol C and Thivel P-X 2013 Evaluation of acoustic emission as a suitable tool for aging characterization of LiAl/$LiMnO_2$ cell *Electrochim. Acta* **88** 488–94
[75] Rhodes K, Dudney N, Lara-Curzio E and Daniel C 2010 Understanding the degradation of silicon electrodes for lithium-ion batteries using acoustic emission *J. Electrochem. Soc.* **157** A1354
[76] Didier-Laurent S, Idrissi H and Roué L 2008 In-situ study of the cracking of metal hydride electrodes by acoustic emission technique *J. Power Sources* **179** 412–6
[77] Jung R, Metzger M, Maglia F, Stinner C and Gasteiger H A 2017 Chemical versus electrochemical electrolyte oxidation on NMC111, NMC622, NMC811, LNMO, and conductive carbon *J. Phys. Chem. Lett.* **8** 4820–5
[78] Hatsukade T, Schiele A, Hartmann P, Brezesinski T and Janek J 2018 Origin of carbon dioxide evolved during cycling of nickel-rich layered NCM cathodes *ACS Appl. Mater. Interfaces* **10** 38892–9
[79] Papp J K, Li N, Kaufman L A, Naylor A J, Younesi R, Tong W and McCloskey B D 2021 A comparison of high voltage outgassing of $LiCoO_2$, $LiNiO_2$, and Li_2MnO_3 layered Li-ion cathode materials *Electrochim. Acta* **368** 137505
[80] Strauss F, Payandeh S, Kondrakov A and Brezesinski T 2022 On the role of surface carbonate species in determining the cycling performance of all-solid-state batteries *Mater. Futures* **1** 023501
[81] Dreyer S L, Kondrakov A, Janek J and Brezesinski T 2022 In situ analysis of gas evolution in liquid- and solid-electrolyte-based batteries with current and next-generation cathode materials *J. Mater. Res.* **37** 3146–68
[82] Wang J *et al* 2022 P2-type layered high-entropy oxides as sodium-ion cathode materials *Mater. Futures* **1** 035104
[83] Jung R, Metzger M, Maglia F, Stinner C and Gasteiger H A 2017 Oxygen release and its effect on the cycling stability of $LiNi_xMn_yCo_zO_2$ (NMC) cathode materials for Li-ion batteries *J. Electrochem. Soc.* **164** A1361–77
[84] Wandt J, Freiberg A T S, Ogrodnik A and Gasteiger H A 2018 Singlet oxygen evolution from layered transition metal oxide cathode materials and its implications for lithium-ion batteries *Mater. Today* **21** 825–33
[85] Metzger M, Strehle B, Solchenbach S and Gasteiger H A 2016 Origin of H_2 evolution in LIBs: H_2O reduction vs. electrolyte oxidation *J. Electrochem. Soc.* **163** A798–809
[86] Yu Y, Ning D, Li Q, Franz A, Zheng L, Zhang N, Ren G, Schumacher G and Liu X 2021 Revealing the anionic redox chemistry in O3-type layered oxide cathode for sodium-ion batteries *Energy Storage Mater.* **38** 130–40
[87] Voronina N, Yaqoob N, Kim H J, Lee K-S, Lim H-D, Jung H-G, Guillon O, Kaghazchi P and Myung S-T 2021 A new approach to stable cationic and anionic redox activity in O3-layered cathode for sodium-ion batteries *Adv. Energy Mater.* **11** 2100901
[88] Guo Y-J *et al* 2021 Boron-doped sodium layered oxide for reversible oxygen redox reaction in Na-ion battery cathodes *Nat. Commun.* **12** 5267
[89] Hwang J-Y, Myung S-T, Choi J U, Yoon C S, Yashiro H and Sun Y-K 2017 Resolving the degradation pathways of the O3-type layered oxide cathode surface through the nano-scale aluminum oxide coating for high-energy density sodium-ion batteries *J. Mater. Chem.* A **5** 23671–80
[90] Dreyer S L, Kretschmer K R, Tripković Đ, Mazilkin A, Chukwu R, Azmi R, Hartmann P, Bianchini M, Brezesinski T and Janek J 2022 Multi-element surface coating of layered Ni-rich oxide cathode materials and their long-term cycling performance in lithium-ion batteries *Adv. Mater. Interfaces* **9** 2101100
[91] Neudeck S, Strauss F, Garcia G, Wolf H, Janek J, Hartmann P and Brezesinski T 2019 Room temperature, liquid-phase Al_2O_3 surface coating approach for Ni-rich layered oxide cathode material *Chem. Commun.* **55** 2174–7
[92] Peng B, Wan G, Ahmad N, Yu L, Ma X and Zhang G 2023 Recent progress in the emerging modification strategies for layered oxide cathodes toward practicable sodium ion batteries *Adv. Energy Mater.* **13** 2300334
[93] Peng B, Chen Y, Wang F, Sun Z, Zhao L, Zhang X, Wang W and Zhang G 2022 Unusual site-selective doping in layered cathode strengthens electrostatic cohesion of alkali-metal layer for practicable sodium-ion full cell *Adv. Mater.* **34** 2103210